ACS APPLIED MATERIALS & INTERFACES

Research Article

Cite This: ACS Appl. Mater. Interfaces 2018, 10, 37981−37993

www.acsami.org

Experimental and Computational Study of the Lithiation of $Ba_8Al_yGe_{46-y}$ Based Type I Germanium Clathrates

Andrew Dopilka,[†] Ran Zhao,[‡] J. Mark Weller,[†] Svilen Bobev,[§] Xihong Peng,[∥] and Candace K. Chan*,[†]

[†]Materials Science and Engineering, School for Engineering of Matter, Transport and Energy, Arizona State University, P.O. Box 876106, Tempe, Arizona 85827, United States

[‡]School of Molecular Sciences, Arizona State University, P.O. Box 871604, Tempe, Arizona 85287, United States

[§]Department of Chemistry and Biochemistry, University of Delaware, Newark, Delaware 19716, United States

[∥]College of Integrative Sciences and Arts, Arizona State University Polytechnic Campus, Mesa, Arizona 85212, United States

Supporting Information

ABSTRACT: In this work, we investigate the electrochemical properties of $Ba_8Al_yGe_{46-y}$ (y = 0, 4, 8, 12, 16) clathrates prepared by arc-melting. These materials have cage-like structures with large cavity volumes and can also have vacancies on the Ge framework sites, features which may be used to accommodate Li. Herein, a structural, electrochemical, and theoretical investigation is performed to explore these materials as anodes in Li-ion batteries, including analysis of the effect of the Al content and framework vacancies on the observed electrochemical properties. Single-crystal X-ray diffraction (XRD) studies indicate the presence of vacancies at the 6c site of the clathrate framework as the Al content decreases, and the lithiation potentials and capacities are observed to decrease as the degree of Al substitution increases. From XRD, electrochemical, and transmission electron microscopy analysis, we find that all of the clathrate compositions undergo two-phase reactions to form Li-rich amorphous phases. This is different from the behavior observed in Si clathrate analogues, where there is no amorphous phase transition during electrochemical lithiation nor discernible changes to the lattice constant of the bulk structure. From density functional theory calculations, we find that Li insertion into the three framework vacancies in Ba_8Ge_{43} is energetically favorable, with a calculated lithiation voltage of 0.77 V versus Li/Li$^+$. However, the calculated energy barrier for Li diffusion between vacancies and around Ba guest atoms is at least 1.6 eV, which is too high for significant room-temperature diffusion. These results show that framework vacancies in the Ge clathrate structure are unlikely to significantly contribute to lithiation processes unless the Ba guest atoms are absent, but suggest that guest atom vacancies could open diffusion paths for Li, allowing for empty framework positions to be occupied.

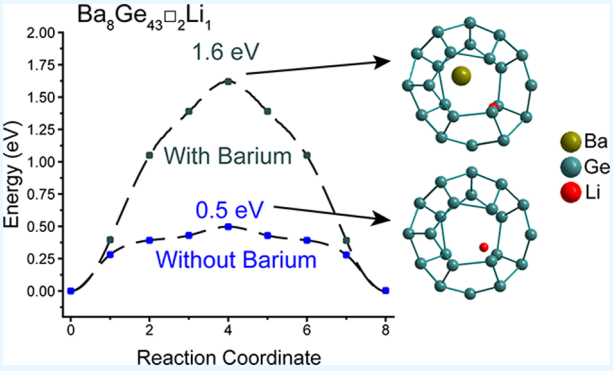

KEYWORDS: *lithium-ion batteries, germanium, clathrate, anode, energy storage*

1. INTRODUCTION

Clathrates[1,2] are known for their unique cage-like structures and their potential as promising superconducting,[3−7] thermoelectric,[8−14] magnetic,[2,15,16] hydrogen storage,[17,18] and hard materials.[19,20] Recently, clathrates have also been investigated as potential electrode materials for Li-ion batteries.[21−29] We have previously investigated the electrochemical properties of ternary type I clathrates based on $Ba_8Al_ySi_{46-y}$ in great detail.[24,29] In our group's prior work, we found that off-stoichiometric silicon clathrates ($8 < y < 12$) displayed capacities corresponding to insertion of ∼40 Li$^+$ per formula unit,[24] whereas materials close to the Zintl condition ($y \approx 16$) displayed very low capacities unless disordered/amorphous surface layers were introduced via ball-milling.[29] On the basis of these results, we hypothesized that Li$^+$ insertion at defects or vacancies could play an important role in the electrochemical properties of clathrates. Interestingly, for all silicon clathrate compositions studied, no electrochemically induced amorphization of the material was observed, and there were no discernible changes to the lattice constant of the bulk structure. This is distinctly different from what occurs during electrochemical lithiation of diamond cubic silicon (c-Si), where a more than 300% change in volume and transformation to amorphous lithium silicide phases are observed.[30]

To further elucidate the electrochemical properties of clathrates, herein we extend our studies to type I clathrates

Received: July 10, 2018
Accepted: October 16, 2018
Published: October 16, 2018

DOI: 10.1021/acsami.8b11509
ACS Appl. Mater. Interfaces 2018, 10, 37981−37993

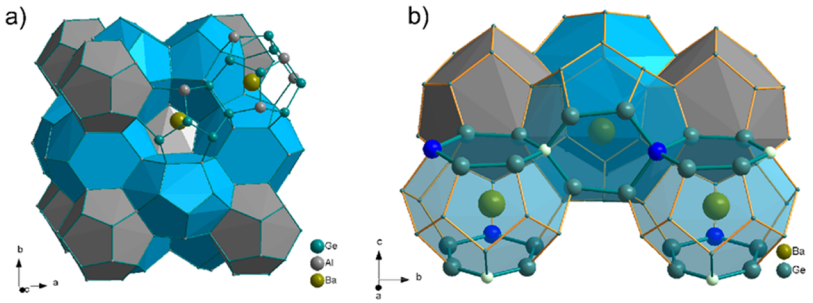

Figure 1. (a) Crystal structure $Ba_8Al_{16}Ge_{30}$. The blue polyhedra are the tetrakaidecahedra with two hexagonal faces and the dodecahedra are shaded gray. (b) Crystal structure of Ba_8Ge_{43} showing the chains of connected hexagons containing vacancies. The dark blue atoms are Ge atoms occupying 6c positions and the white atoms represent the positions of the vacancies, also at the 6c sites.

based on $Ba_8Al_yGe_{46-y}$ and explore the effect of defects in the clathrate structure on the lithiation behavior using experimental and first-principles density functional theory (DFT) investigations. Similar to the aforementioned silicon clathrates studied previously, the structure of these germanium clathrates is made up of two pentagonal dodecahedra (Ge_{20}) and six tetrakaidecahedra (Ge_{24}) per unit cell (Figure 1a), crystallizing in the $Pm\bar{3}n$ (223) space group. Each Ge_{20} cage is composed of 12 pentagonal faces, while the Ge_{24} cages are made up of 12 pentagonal and 2 hexagonal faces. The Ba guest atoms are found at the 6d and 2a sites in the center of the Ge_{24} and Ge_{20} cavities, respectively, while the Ge and Al atoms occupy the framework sites at the 6c, 16i, and 24k positions as described by Wyckoff symmetry notation.[31,32] The framework substitution of Ge by Al atoms enables the structure to be rationalized by the Zintl concept, where each element achieves a (nearly) closed-shell electronic configuration.[33]

Ge clathrate frameworks have been shown to be able to accommodate vacancies and even Li atoms. For example, to compensate the excess electrons donated to the framework from the Ba atoms, Ba_8Ge_{46} (but not Ba_8Si_{46}) can spontaneously form three vacancies in the 6c positions to form $Ba_8Ge_{43}\square_3$, where $\square$ is a vacancy (from now on referred to as Ba_8Ge_{43})[34] (Figure 1b). Framework vacancies have also been reported in the ternary $Ba_8Al_yGe_{46-y}$ ($4 \le y \le 16$) clathrates.[32] Electrochemical Li insertion into these framework vacancies has to our knowledge, not been reported, but clathrate compounds containing Li framework substitution, for example, $K_8Li_yGe_{46-y}$ ($0 \le y \le 2.3$), have been synthesized.[35−37] Li framework substitution is particularly interesting because it suggests that there are defined, stable Li positions in the clathrate structure; however, if Li movement between these positions is possible has yet to be addressed. In this work, we investigate the electrochemical properties of $Ba_8Al_yGe_{46-y}$ (y = 0, 4, 8, 12, 16) clathrates synthesized by arc-melting. We find that all of the compositions undergo two-phase reactions to form Li-rich amorphous phases, similar to the transformations seen in diamond structured Si (c-Si) and certain forms of diamond Ge (c-Ge).[38−41] This is distinctly different from the Si clathrate analogues, which do not transform to amorphous phases during the electrochemical reaction. A composition dependence on the capacity and reaction voltage is seen with changes in the Al framework substitution. It is also found that ball-milling significantly amorphized the clathrate structure as determined using X-ray diffraction (XRD) and transmission electron microscopy (TEM). Si clathrates subjected to the same ball-milling conditions did not display as much amorphous phase formation,[29] suggesting that the Ge framework is less structurally stable. Electrochemical impedance spectroscopy (EIS) is used to confirm the presence of Warburg diffusion of Li^+ in the amorphous phases by inspection of the Bode plots in the low-frequency region.

Finally, we investigate the possibility of Li insertion into the clathrate structure prior to the two-phase reaction with XRD and first-principles DFT calculations. Single-crystal XRD (SCXRD) results indicate the presence of vacancies in clathrates with low Al content. From DFT calculations, we find that Li insertion into the three framework vacancies in Ba_8Ge_{43} is energetically favorable at a calculated lithiation voltage of 0.77 V versus Li/Li^+. However, the calculated energy barrier for Li diffusion between vacancies is 1.6 eV, which is too high for significant room-temperature diffusion. If Ba is removed from the Ge_{24} cage, the activation barrier decreases to 0.5 eV, indicating that the guest atom impedes Li motion. DFT also predicts an increase in lattice constant after insertion of the 3 Li into the vacancies; however, ex situ XRD shows no increase in lattice constant before or during the onset of the two-phase reaction, suggesting no Li incorporation into the vacancies. These results show that framework vacancies are unlikely to have a significant impact on the capacity of the clathrates but do suggest that guest atom vacancies could open diffusion paths for Li, allowing for empty framework positions to be occupied.

2. EXPERIMENTAL SECTION

2.1. Synthesis of $Ba_8Al_yGe_{46-y}$ Clathrates. A series of clathrates with composition of $Ba_8Al_yGe_{46-y}$ (y = 0, 4, 8, 12, 16) were synthesized using arc-melting (Supporting Information). The samples were named according to Aly, where y represents the nominal amount of Al, for example, Al16 means y = 16 or $Ba_8Al_{16}Ge_{30}$. The as-made, arc-melted ingots were processed further: HG-Aly refers to the sample ground by hand using a mortar and pestle, while BM-Aly refers to the HG-Aly sample after ball-milling.

2.2. Materials Characterization. The clathrate samples were characterized using SCXRD and powder X-ray diffraction (PXRD), X-ray photoelectron spectroscopy (XPS), scanning electron microscopy (SEM), and TEM. Composite electrodes containing the clathrate powders, carbon black, and binder on copper foils were evaluated in half cells with Li metal counter electrodes and nonaqueous electrolyte. More details about the materials and electrochemical measurements are described in the Supporting Information.

2.3. Computational Methods. First-principles DFT calculations were performed in a similar manner as in our previous work[25] and are described in more detail in the Supporting Information. The formation energies, Gibbs free energy change, and average lithiation voltages were calculated as described previously.[25] The climbing image nudged elastic band (NEB) method was used to calculate the Li diffusion barriers.[42]

DOI: 10.1021/acsami.8b11509
ACS Appl. Mater. Interfaces 2018, 10, 37981−37993

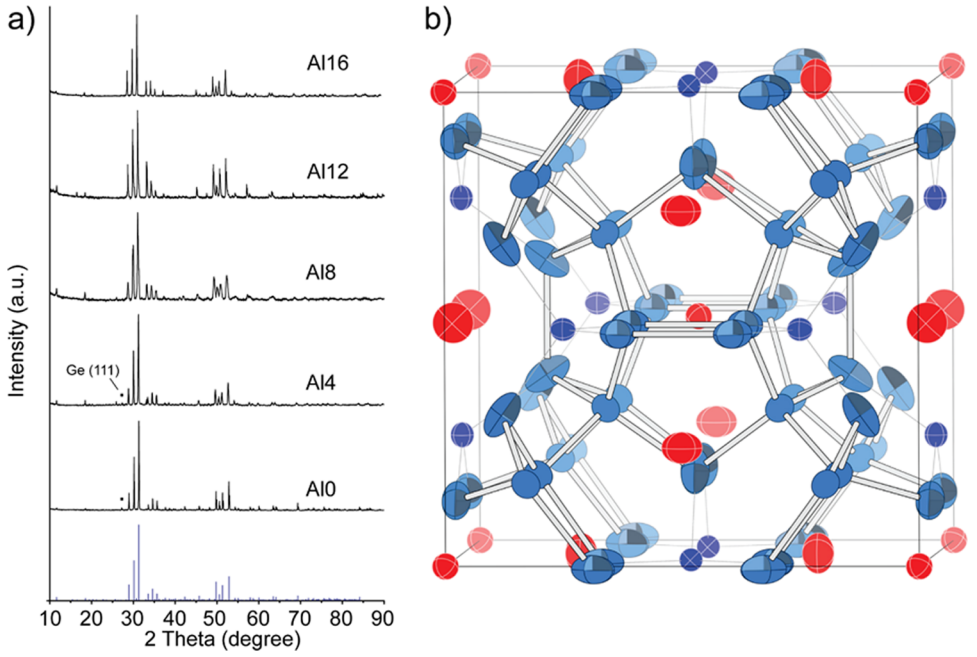

Figure 2. (a) PXRD patterns of hand-ground Ge clathrates with reference pattern PDF 01-073-5638 corresponding to Ba_8Ge_{43} on the bottom; (■) c-Ge. (b) Representation of the $Ba_8Al_yGe_{46-y}$ (y = 4) structure with anisotropic displacement parameters. The thermal ellipsoids are drawn at the 90% probability level, where the Ba atoms are colored in red and the Ge/Al framework positions are differentiated as follows: 24k sites are represented with light blue ellipsoids with octant shading; the 16i sites are shown as light blue outline ellipsoids, and the 6c sites are in dark blue (with the principal ellipses shown). The data are obtained from the single-crystal refinement for sample Al4. The distinctive shape of the ellipsoid of the atoms occupying the 24k sites is indicative of small positional disorder—a direct consequence of vacancies present at the neighboring 6c sites.

3. RESULTS AND DISCUSSION

3.1. Structural Characterization. PXRD patterns were taken on the synthesized Ge clathrates samples before and after ball-milling. All of the hand-ground samples displayed crystalline peaks (Figure 2a), matching the reflections for Ba_8Ge_{43} clathrate (PDF 01-073-5638),[34] and in excellent agreement with the simulated PXRD patterns from the refined structures via SCXRD methods. For the Al containing samples, the reflections were shifted to lower angles and least-squares refinement showed the lattice constant increased from 10.653 Å for Al0 to 10.835 Å for Al16 (Table S1). These cell parameters match closely with those previously reported[32] as well as the SCXRD results (Table 1). Crystalline diamond cubic Ge (c-Ge), identified by the (111) reflection, was noticeable in the PXRD patterns for Al0 and Al4, but the phase fraction determined from the refinement showed that the quantity was very small (Table S1). No other crystalline peaks were observed. The powder after ball-milling (Figure S1a) also displayed a crystalline clathrate structure without any change of the cell parameter and impurities, but the PXRD diffraction intensities decreased and the peaks were broader, which is consistent with a smaller particle size in the ball-milled samples.

Table 1. Lattice Parameter and Ge/Al Ratio on Each Framework Site (6c, 16i, and 24k) as Determined from SCXRD Studies

sample name	nominal composition	a-parameter (Å) from SCXRD	Ge/Al ratio		
			6c	16i	24k
Al0	Ba_8Ge_{43}	10.6335(15)	N/A	N/A	N/A
Al4	$Ba_8Al_4Ge_{42}$	10.7411(10)	5.4:61.3[a]	9:1	~100:0
Al8	$Ba_8Al_8Ge_{38}$	10.8008(5)	1:99	69:31	98:2
Al12	$Ba_8Al_{12}Ge_{34}$	10.8385(17)	8:92	60:40	92:18
Al14	$Ba_8Al_{14}Ge_{32}$	10.8425(6)	18:82	62:38	86:14
Al16	$Ba_8Al_{16}Ge_{30}$	10.819(3)	30:70	69:31	74:26

[a]The balance to 100% occupancy is attributed to vacancies.

SCXRD was performed on the as-synthesized clathrate samples by extracting small crystallites from the crushed arc-melted ingots. The lattice parameters and Ge/Al ratios obtained from the SCXRD data are shown in Table 1 and the crystallographic information files can be found in the Supporting Information. Standard deviations on the occupancies were 1% or better. The four samples with the highest Al content (Al8−Al16) showed unit cell parameters in the narrow range of 10.8008(5) to 10.8425(6) Å and refined compositions of $Ba_8Al_{11.4(1)}Ge_{34.6(1)}$ to $Ba_8Al_{15.6(1)}Ge_{30.4(1)}$.

The structure refinements for almost all prepared clathrates showed excellent agreement between the nominal (loading) and final composition, which is indirect proof for the homogeneity of the samples. The unit cell volumes subtly decrease with the decrease of the Al content, corresponding to the small difference in the elemental radii (Al is 1.248 Å while Ge is 1.242 Å), but the variations in the unit cell volume were not monotonic. Because Al and Ge atoms scatter X-rays in a significantly different way, the refinements of the occupancies of Al on the three framework positions was possible and confirmed the preference of Al for the 6c site. This is in contrast to the $Ba_8Al_ySi_{46-y}$ clathrates, where the exact Al/Si ratios on the individual framework sites cannot be reliably established using X-rays.[43,44] The ratios are in agreement with the literature on other type I clathrates, where the preference for the 6c site is well documented.[45,46]

DOI: 10.1021/acsami.8b11509
ACS Appl. Mater. Interfaces 2018, 10, 37981−37993

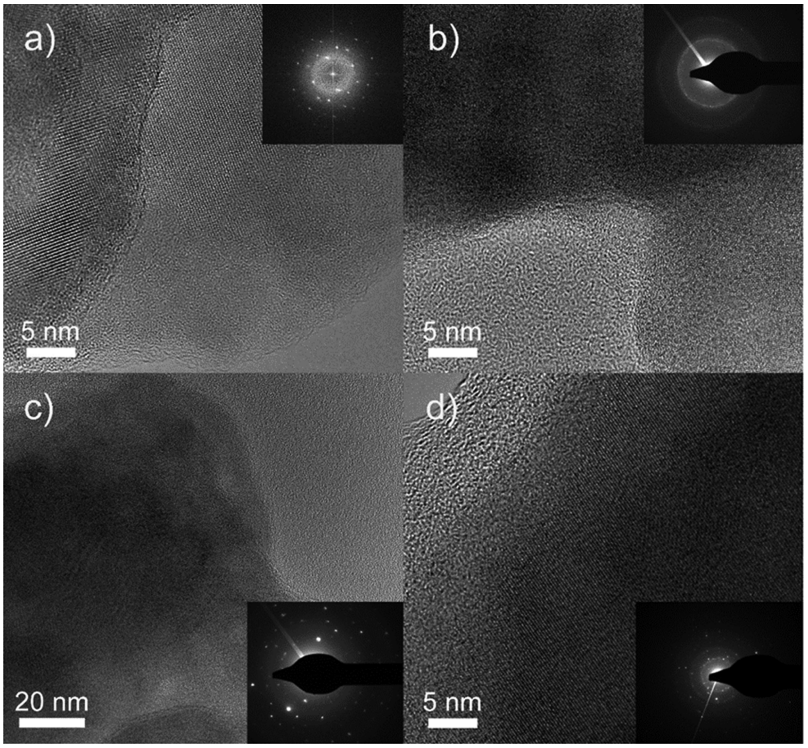

Figure 3. High-resolution TEM and SAED of Ge clathrates (a) HG-Al0, (b) BM-Al0, (c) HG-Al16, and (d) BM-Al16.

For the sample with the lowest Al content (Al4), the 24k site appeared to contain no measurable amount of Al; the 16i site was co-occupied by Ge and Al in a ratio of 9:1, and for the first time, the 6c site in a Ba−Al−Ge clathrate system was found to be under-occupied—when freed, the site occupation factor of this position was less than 100%, suggesting that the atom(s) located at 6c is almost 1/4 lighter than Al. This, together with the drastic decrease in the unit cell parameter (a = 10.741 Å), is an indicator of vacancies at the 6c site. The diffraction data can then be modeled with ca. 2 vacancies at the 6c site. This results in a refined composition of $Ba_8Al_{\sim 6}Ge_{\sim 38}$, which is in good but not excellent agreement with the nominal composition of $Ba_8Al_4Ge_{42}$. This structural description is consistent with the interatomic distances within the framework, which for the Al-rich samples show Ge/Al (6c)−Ge/Al (24k) bond lengths exceeding 2.51−2.53 Å (recall that the 6c site is mostly occupied by Al, which is spatially more demanding than Ge), while for Al4, the corresponding bond distance is 2.4660(9) Å.

The anisotropic displacement parameters of the Ge atoms neighboring the vacancies (i.e., in the 24k sites) are also worthy of a mention—instead of spherical, the mean square atomic displacements (0.0273, 0.0141, and 0.0140 Å^2) show that one of the principal directions is nearly twice as large as the other two. This is also readily seen in Figure 2b, where the nearest Ge/Al neighbors at the 24k site are strongly affected by the vacancy, causing the ellipsoid to be elongated in the direction of the Ge/Al (6c)−Ge/Al (24k) bond.

Exactly the same phenomenology concerning the bond distances and anisotropic displacement parameters is also seen in the structure refinements for Al0, Ba_8Ge_{43}. The unit cell parameter decreased sharply to 10.6335(15) Å with the 6c site being vacant nearly 50% of the time. As a result, the unrealistically short Ge−Ge distance of 2.354(1) Å is avoided. The anisotropic displacement parameter of the Ge atoms neighboring the vacancies is also clear indication that these atoms are "vibrating" around their equilibrium positions—the principal direction is nearly three times as large as the other two, as evident from the principal mean square displacements of 0.0510, 0.0160, and 0.0153 Å^2. The latter is a sign that the structural description of the Al0 clathrate in the same space group as the others leads to structural deficiencies and alternatives must be sought. Other research teams have shown that using an eight times larger unit cell volume with cell edge in excess of 21 Å and body-centered cubic symmetry might resolve these problems,[34,47,48] although the diffraction patterns of our arc-melted samples did not show reflections that violate the presumed symmetry.

3.2. XPS Characterization. XPS was used to further characterize the surfaces of the hand-ground and ball-milled clathrate electrodes. Deconvolution of the high-resolution Ge 2p spectrum (Figure S2a), showed characteristics typical for GeO_2, GeO, and Ge−Ge at binding energies of 1220.8, 1219.2, and 1217.8 eV, respectively.[49] From the fitting procedure, the amount of Ge−Ge signal was found to be 9% for Al0 and 15% for Al16 in both HG and BM cases (Table S2). To serve as a reference, c-Ge powder was ball-milled and characterized by XPS; the Ge−Ge contribution was 21% of the total Ge 2p signal (Table S2). This suggests that the oxide layer on the Ge clathrates is thicker than the native oxide layer on c-Ge. A similar observation was made in epitaxially grown Ge clathrate, where only the Ge oxide signals were seen in the Ge 2p XPS spectrum taken from the surface.[50] The high-resolution XPS profile for Al 2p (Figure S2b) showed a single peak at 75.44 and 75.07 eV for BM-Al16 and HG-Al16, respectively. These binding energies are in the range for aluminum oxide.[51] Because of the care taken to minimize oxygen contamination during the arc-melting synthesis, the oxidized surfaces likely formed from the exposure of the germanium clathrates to atmospheric oxygen.

DOI: 10.1021/acsami.8b11509
ACS Appl. Mater. Interfaces 2018, 10, 37981−37993

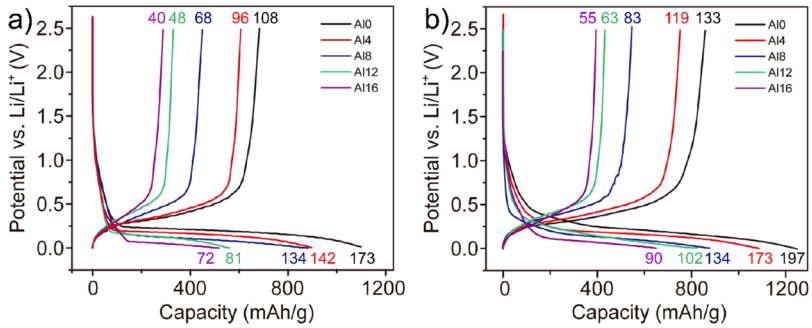

Figure 4. Galvanostatic voltage curves obtained from the first cycle for (a) HG and (b) BM samples. Numbers indicate the equivalent number of Li per formula unit of clathrate.

3.3. SEM and TEM Characterization. SEM was used to characterize the morphology of the pristine electrodes prepared from hand-ground (Figure S3) and ball-milled clathrates (Figure S4). The SEM micrographs of the HG samples show large shards (greater than 3 μm) of clathrate particles covered in carbon black. The BM samples contained spherically shaped particles generally around 1 μm or smaller in diameter, demonstrating that ball-milling changed the morphology and particle sizes. No morphological differences were observed between the clathrates of varying Al substitution.

TEM was used to characterize the surfaces and crystallinity of the hand-ground and ball-milled Al0 and Al16 samples (Figure 3). Selected area electron diffraction (SAED) was also used to assess the crystallinity of an entire particle. Similar to our previous work with the $Ba_8Al_ySi_{46-y}$ clathrates, we find that ball-milling has a considerable effect on the crystallinity of the samples, particularly at the surface. For HG-Al0, distinct lattice fringes and a spot pattern in the fast Fourier transform (FFT, inset) were observed, indicating crystalline clathrate in the center of the particle, although with a thick amorphous layer (up to ~15 nm) on the surface (Figure 3a). The amorphous layer on the surface of the particles is consistent with the oxide layer observed in the XPS results. From the TEM image, small crystalline regions could be seen in the BM-Al0 particles, but the SAED pattern showed diffuse rings, indicating that the particle lacked long range order and contained large amorphous content (Figure 3b). This indicates that the ball-milling process significantly amorphized the Al0 clathrate particles, which is consistent with the lower and broader intensities from the PXRD patterns of the ball-milled powders (Figure S1a).

For the Al16 samples, a similar trend is seen whereby HG-Al6 (Figure 3c) is more crystalline than BM-Al16 (Figure 3d) based on the SAED patterns of the particles. The BM-Al16 sample appears to have retained more of its crystallinity after the ball-milling based on the decreased amount of amorphous background in the SAED compared with BM-Al0. This is consistent with the XRD pattern (Figure S1a) where BM-Al16 had sharper and more intense reflections than the BM-Al0 pattern, suggesting a higher crystallinity for BM-Al16.

3.4. Galvanostatic Measurements. To study the electrochemical properties of the Ge clathrate samples, galvanostatic cycling was performed between 0.01–2.5 V versus Li/Li^+ at 25 mA/g. The first charge (lithiation) and discharge (delithiation) voltage curves are shown in Figure 4. As indicated by the voltage plateaus observed during charging, the clathrates undergo two-phase conversion reactions[52] to form Li-rich phases, with a large amount of Li reacted per clathrate formula unit (f.u.), as designated by the numbers next to each voltage profile. For example, HG-Al0 (Ba_8Ge_{43}) reacted with 173 Li per f.u. in the first charge, which corresponds to 4 Li/Ge (assuming all of the charge went toward the lithiation reaction with the clathrate). However, because of the irreversible capacity loss in the first cycle, there is likely substantial solid electrolyte interphase (SEI) formation from electrolyte reduction and the actual Li/Ge ratio is lower.

It is well known that c-Ge will react with Li to form a series of amorphous and crystalline Li–Ge phases, accompanied by a large volume expansion.[39] In contrast to c-Ge, which reacts at ~350 mV versus Li/Li^+,[39,53,54] we find that the reaction potential for the clathrates occurs at a lower voltage (~160–200 mV for HG-Al0) and decreases with the increasing amount of Al content. The capacity of the first charge also decreases with the increasing Al content, suggesting that framework substitution of Al alters the properties of the two-phase reaction. The voltage profiles are more sloped in the ball-milled samples (Figure 4b) than in the hand-ground ones (Figure 4a), which is consistent with the higher amount of amorphous content in the ball-milled powders because lithium is expected to react with the amorphous clathrate phase in a solid-solution mechanism, similar to lithiation of amorphous Si and Ge.[54,55]

The delithiation characteristics for the HG and BM samples are similar and show a gradually sloping voltage profile, indicating a single-phase reaction. The voltage profiles of the subsequent cycles were also sloped (as shown in Figure S5a for HG-Al0). These observations are similar to those found in lithiation of c-Si and c-Ge, whereby amorphous lithium silicide/germanide phases grow at the expense of the unlithiated crystalline phase as the electrochemical reaction proceeds in the first charge, but subsequent cycling involves lithium insertion/deinsertion into the amorphous phases in a solid-solution mechanism. XRD of the electrodes at the end of the first charge (Figure S1b) showed no reflections, which suggests that the phases after lithiation are amorphous. This is different from the lithiation of Ge and type II $Na_{24}Si_{136}$ clathrates, where the formation of Li containing crystalline phases is observed at low voltages.[23,39] These ex situ XRD results suggest that the presence of Ba and Al seem to impede the formation of these phases in Ge clathrates, although operando studies would be more suitable for detecting the presence or absence of transient Li–Ge phases.[39] The capacities also increase after ball-milling, which can be attributed to enhanced lithiation in the smaller particle sizes

DOI: 10.1021/acsami.8b11509
ACS Appl. Mater. Interfaces 2018, 10, 37981–37993

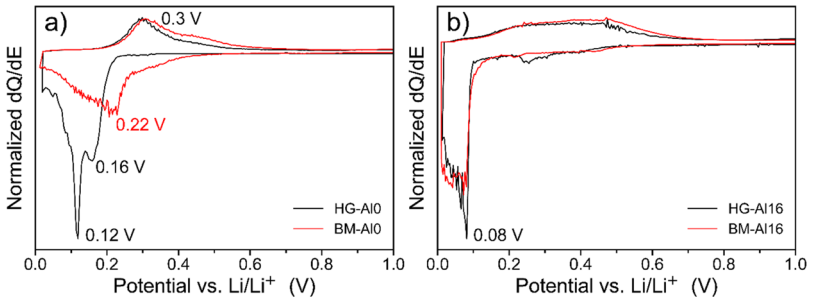

Figure 5. Differential capacity plots of the first cycle of (a) ball-milled and hand-ground Al0 and (b) ball-milled and hand-ground Al16 from galvanostatic cycling at 25 mA/g.

due to the decreased diffusion length, as observed in the SEM images (Figures S3 and S4).

The differential capacity (dQ) plots for Al0 and Al16 (Figure 5), derived from galvanostatic cycling, are presented to elucidate the differences between the HG and BM voltage profiles. The reduction peaks are attributed to the two-phase reaction between the unlithiated Ge clathrate and the amorphous Li germanide phases. The HG-Al0 dQ plot (Figure 5a) displayed two sharp reduction peaks at 0.16 and 0.12 V versus Li/Li$^+$, suggesting the formation of a series of Li germanide phases with different compositions. This potential-dependent redox behavior is distinctly different from that in c-Ge, where peaks at ∼0.35 and ∼0.18 V are seen in dQ plots during lithiation.[39,54] The BM-Al0 sample, however, shows a much broader voltage profile with the reactions starting at ∼0.4 V in contrast to ∼0.2 V for HG-Al0. This is consistent with the large amount of amorphous content in BM-Al0, as seen in the TEM results (Figure 3b) and the tendency for amorphous materials to display a much wider reaction window because of a larger distribution of possible Li reaction site energies.[56] Upon delithiation, both BM and HG-Al0 show similar behavior with an oxidation peak at 0.3 V, suggesting that the phases created at the end of lithiation are similar. The dQ plots for HG and BM-Al16 match closely with each other (Figure 5b), indicating that the ball-milling did not significantly affect the electrochemical properties. This is consistent with the TEM and XRD results showing that the BM-Al16 retained more of its crystallinity than BM-Al0. The reaction begins at 0.08 V in the Al16 samples, demonstrating a decrease in the reaction voltage as the Al content increases. The delithiation of Al16 is characterized by a broad peak stretching from 0.15 to 0.6 V, which contrasts with the sharper profile observed in Al0. We attribute this to the distribution of Al over many possible configurations in the amorphous phase, which would result in the reaction voltage to be more spread out, reflecting the different possible chemical environments for Li. The dQ plots of subsequent cycles (Figure S6) showed little change in the potential-dependence behavior, with broad reaction peaks characteristic of the lithiation of amorphous phases.

The capacity retention plots for the HG samples (Figure S5b) showed that the capacity of the Al0, Al4, and Al8 clathrates quickly decreased to less than 5% of their initial lithiation capacity while Al12 and Al16 retained 10 and 20%, respectively, of the initial capacity after 20 cycles. The results also show that Al16 showed the highest capacity retention, but lowest charge capacity in the first cycle. Al12 and Al16 react with the least amount of Li and thus suffer less from the volume expansion induced capacity degradation during cycling. The Coulombic efficiency (CE) of the first cycle for the BM and HG samples (Figure S5c) decreases with the increasing Al content and is also higher for the ball-milled samples.

This quick capacity fade is typical of unoptimized Si and Ge electrodes and arises due to large volume changes during charge and discharge, which can cause particle decrepitation/pulverization and detachment from the current collector.[30,57,58] Our electrode preparation (Supporting Information) is not optimized for large volume expansion, as generally more conductive additives are used to maintain electronic contact.[59] Ge powder that was ball-milled was also tested and a similar capacity fade was observed (Figure S7). Therefore, this low capacity retention could be due to the pulverization and particle detachment of the clathrate materials after the amorphization reaction and hence could be improved with subsequent modification of the electrode formulation and particle sizes.

The composition dependence of the capacity can be rationalized by considering the electrochemical behavior of Li with Ge versus Al. Al reacts with 1 Li to form the LiAl phase at room temperature,[60] while Ge can react with up to 4.4 Li.[54] This means that replacing Ge with Al will decrease the capacity of the resulting amorphous phase. In Table S3, the theoretical and observed experimental capacities are compared assuming reaction of 4.4 Li/Ge. Note that to understand the effect of composition to the observed capacities, the contribution of charge to SEI formation is not considered. Al0 shows the closest correspondence to the theoretical values, but as the Al content increases, the difference between theoretical and experimental values increases. Previous studies on amorphous Si−Al-sputtered thin films[61] have suggested that the formation of ternary phases, such as LiAlSi,[62] may trap Li and limit the lithiation. LiAlGe also exists, but its electrochemical properties have not been investigated. The formation of a kinetically trapping phase could also explain the lower CE found for the clathrates with higher Al content (Figure S5c). However, no other crystalline phases are detected after lithiation (Figure S1b), indicating that if present, any crystalline regions are too small to detect via XRD. Different SEI formation properties could also contribute to this trend in the CE. The presence of Ba in these amorphous phases further complicates the analysis and more detailed studies would be needed to understand the properties and formation of the amorphous phases.

3.5. Post-Mortem Characterization. As discussed previously, PXRD of the electrodes after the first charge showed that the reflections associated with the clathrates had all disappeared, suggesting the amorphization of the material and a conversion reaction mechanism (Figure S1b). Comparing the morphology of the clathrate electrodes before and after

DOI: 10.1021/acsami.8b11509
ACS Appl. Mater. Interfaces 2018, 10, 37981−37993

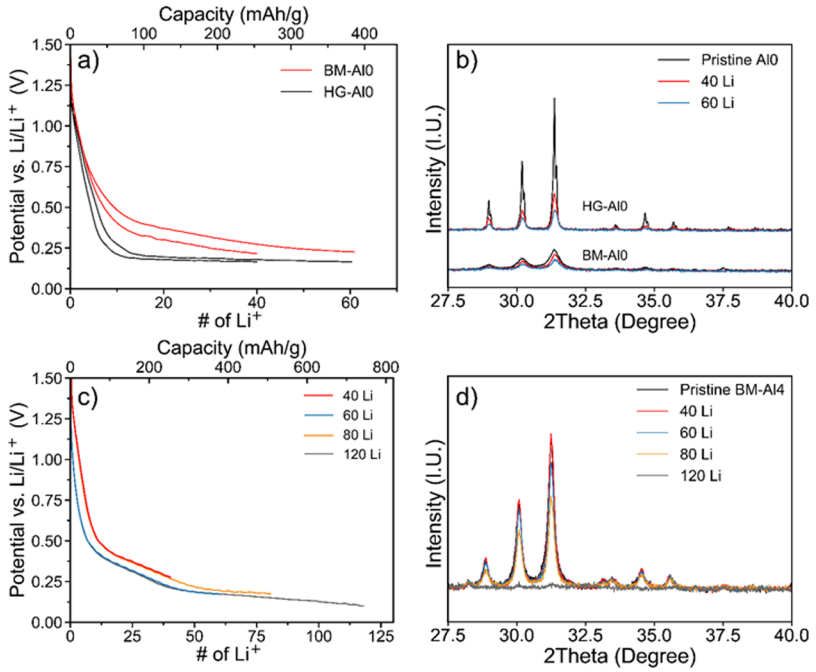

Figure 6. Voltage profiles (galvanostatic charging at 25 mA/g) of the electrodes to specific degrees of lithiation (left) and corresponding PXRD patterns obtained after the lithiation (right) for (a,b) HG and BM-Al0, (c,d) BM-Al4.

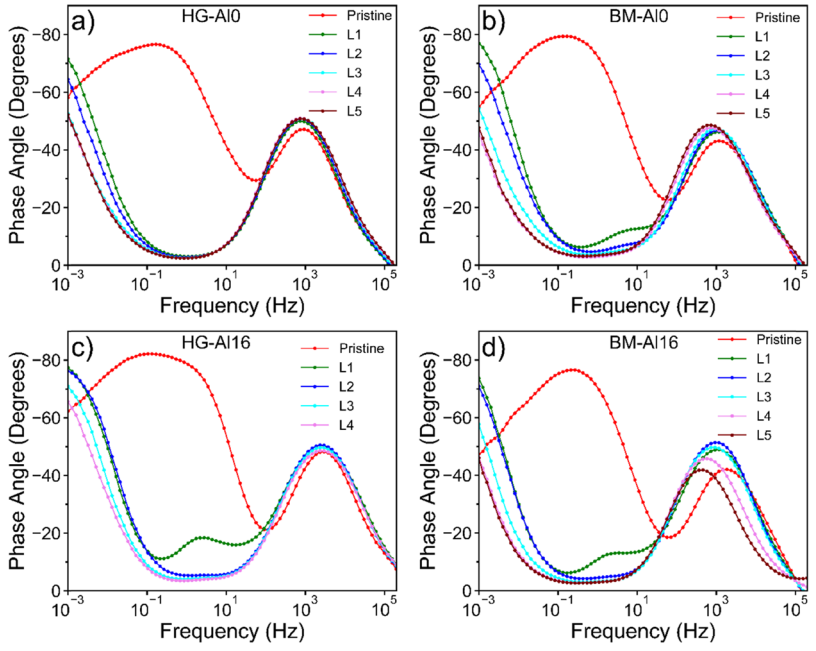

Figure 7. Bode plots showing the phase angle vs frequency for (a) HG-Al0, (b) BM-Al0, (c) HG-Al16, and (d) BM-Al16 obtained at different SOC, where L1 is the lowest SOC and L5 is the highest. The lithiation capacities for each SOC are shown in Figure S8.

the first lithiation (Figure S4) showed indication of particle volume expansion and coating of the electrode with an SEI layer, which explains the fast decay of the capacities (Figure S5b) and generally low CE (Figure S5c,d).

These results confirm that the reaction mechanism of Li with the Ge clathrates is a conversion reaction to a Li-rich phase like that seen in the electrochemical lithiation of c-Si and c-Ge. However, the question of whether Li insertion into the crystal structure is possible is still yet to be answered. The voltage region before the start of the voltage plateau is considerably more sloped for the BM samples, indicating a single-phase reaction.[52] Ex situ PXRD was performed for the BM and HG samples before and after the beginning of this region, which corresponds to 40 and 60 Li inserted per f.u. (with the assumption that all the charge went towards Li insertion), to assess the crystallinity at these points in the lithiation process. The voltage profiles and corresponding XRD results from these experiments are shown in Figure 6a,b.

For the pristine (unlithiated) electrodes, the HG-Al0 sample is more crystalline when compared to the BM sample, as seen by the higher intensity and sharper reflections. This is also consistent with the TEM characterization results (Figure 3).

DOI: 10.1021/acsami.8b11509
ACS Appl. Mater. Interfaces 2018, 10, 37981−37993

After insertion of 40 Li per f.u., the intensities of the clathrate reflections in the XRD decreased in both Al0 samples, but by different amounts. The intensity of the reflections in HG-Al0 decreased by more than half, while that for BM-Al0 decreased to ~75% of those in the pristine sample. After insertion of 60 Li, the reflections decreased more for both samples. The larger decrease in peak intensity for HG-Al0 suggests that the Li being inserted is participating in the two-phase conversion reaction between the Ge clathrate and the Li-rich amorphous phase, thus decreasing the amount of crystalline clathrate. This is corroborated by the flat voltage profile at this point in the first lithiation step (Figure 6a). The voltage profile for BM-Al0, however, is more sloped indicating a solid-solution insertion into an amorphous phase,[55,63] which in this case is the amorphous clathrate phase that was formed during ball-milling. BM-Al4 was investigated in a similar manner (Figure 6c,d). After insertion of 40 Li per f.u., no decrease in the intensity of the clathrate reflections was detected. This suggests that these Li were not participating in a two-phase conversion of the crystalline clathrate, but a reaction with the amorphous surfaces (i.e., the surface oxides, the amorphous layer formed from ball-milling). As more Li was inserted, the clathrate structure was completely converted to the amorphous phase at around 120 Li per f.u. No significant change in peak positions was seen after the insertion of these different amounts of Li, suggesting that the clathrate structure was maintained without large change in lattice constant until the conversion reaction.

The PXRD results were confirmed with SCXRD measurements on samples after lithiation. Al0 powders were chemically lithiated using direct contact with Li foil, but the refinement results showed no statistically significant differences from the lattice constant and formula of the as-synthesized Al0 (Supporting Information).

3.6. Electrochemical Impedance Spectroscopy. In our previous investigation of Si clathrates, EIS was used to identify the mechanism of lithiation as being confined to the surface of the particles in a pseudocapacitive-faradaic process, primarily by inspection of the Bode plots.[29] The same galvanostatic pulse protocol we used in that study was applied to both the hand-ground and ball-milled Al0 and Al16 Ge clathrate samples (Supporting Information, Figures S8–S11). In the Bode plot, the low-frequency phase angle close to −45° is an indication of Warburg-type, solid-state diffusion of Li into the electrode, while a phase angle close to −90° would indicate a blocking electrode or surface adsorption of Li.[64] As shown in Figure 7, the low-frequency angle moved toward −45° for all samples as the state-of-charge (SOC) increased, which is consistent with the conversion of the crystalline clathrate into amorphous phases that can react with lithium. When comparing the Bode plots for HG-Al0 (Figure 7a) with HG-Al16 (Figure 7b), we see that the phase angles for HG-Al16 remained less than −60°, indicating a more blocking character. This is also consistent with the increased crystallinity of the pristine sample as observed by TEM, as well as the lower lithiation capacities obtained in the galvanostatic cycling. On the other hand, the phase angle at low frequencies remained close to −80° for silicon clathrates lacking an amorphous surface layer,[29] indicating the blocking character of the structure. We attribute the Warburg feature to Li diffusion in the amorphous phases present in the Ge clathrates, which originate from the decreased structural stability of the Ge clathrates to atmospheric oxygen, ball-milling, and also to electrochemically induced amorphization, while the blocking character of the electrodes originate from the crystalline clathrate domains.

The reaction mechanism for the hand-ground and ball-milled Ge clathrate samples can thus be summarized as follows. After reduction (presumably) of the surface oxide species and formation of the SEI layer, the Li reacts with the HG clathrate in a two-phase reaction between the unlithiated crystalline clathrate and a Li-rich amorphous germanide phase. For the BM samples, lithium insertion into the amorphous layer on the outside of the crystalline cores (presumably arising from the damage caused by ball-milling) precedes the two-phase reaction. For both cases, full lithiation results in complete amorphization, with subsequent lithium cycling occurring through a single-phase, amorphous solid-solution.

3.7. Theoretical Calculations. DFT was used to theoretically investigate the lithiation voltages and diffusion barriers (Supporting Information) for the Al0 and Al16 Ge clathrates to rationalize why Li insertion into the clathrate structure is not observed experimentally unless it is amorphous. The framework vacancies can occupy the 6c position in a random or ordered arrangement depending on the synthesis conditions and heat treatment.[6,34] For arc-melted Ba_8Ge_{43}, it has been reported that there is an absence of vacancy ordering[6] and this is consistent with single-crystal refinements of the arc-melted Al0 clathrates synthesized in this work (Supporting Information). For this reason, we chose to model Ba_8Ge_{43} with randomly chosen vacancies at the 6c positions in the conventional unit cell. For the Al16 clathrate, we followed previous calculations showing that the lowest energy configuration consists of 3 Al at the 6c sites, 1 Al at a 16i site, and 12 Al in the 24k sites, with no Al–Al bonds.[32,65] The formation energy and lattice constants for the unlithiated structures are shown in Table 2. The lattice constants match well with the experimental results and show the increase of lattice constant with substitution of 16 Ge with Al.

For Li insertion to occur in a material, there must be favorable positions in the crystal structure for Li to reside and a low-energy pathway between these positions for bulk diffusion. To assess the possibility of Li insertion into the Ge clathrates,

Table 2. Calculated Formation Energies, Gibbs Free Energy Changes, Voltages, and Lattice Constants of Unlithiated and Lithiated Compounds[a]

composition	formation energy (eV/atom)	Gibbs free energy change (eV)	average lithiation voltage (V)	lattice constant (Å)
$Ba_8Ge_{43}\square_3$	−0.216	N/A	N/A	10.83
$Ba_8Ge_{43}\square_2Li_1$ (6c)	−0.228	−0.85	0.85	10.88
$Ba_8Ge_{43}Li_3$	−0.247	−2.31	0.77	11.02
$Ba_8Ge_{43}\square_3Li_1$ (6b)	−0.203	0.48	−0.48	10.90
$Ba_8Ge_{43}Li_3Li_1$ (6c + 6b)	−0.241	0.10	−0.10	11.05
$Ba_8Al_{16}Ge_{30}$	−0.303			10.95
$Ba_8Al_{16}Ge_{30}Li_1$ (6b)	−0.288	0.53	−0.53	10.98
$Ba_8Al_{16}Ge_{30}Li_1$ (off pentagon in Ge_{24})	−0.286	0.63	−0.63	10.99

[a]Parentheses after the composition indicate the site(s) occupied by the Li. All calculations used bcc Li and the respective unlithiated clathrate as reactants except those for $Ba_8Ge_{43}Li_3Li_1$ (6c + 6b), which used bcc Li and $Ba_8Ge_{43}Li_3$ reactants.

DOI: 10.1021/acsami.8b11509
ACS Appl. Mater. Interfaces 2018, 10, 37981–37993

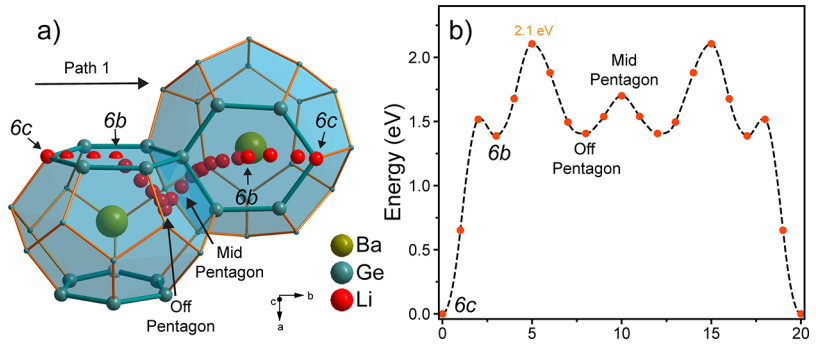

Figure 8. (a) Schematic of two connected tetrakaidecahedra showing the Li positions of Path 1 where the starting and ending points consist of Li in vacancies at the 6c position (white atom indicates unfilled vacancy). (b) NEB energies of Path 1.

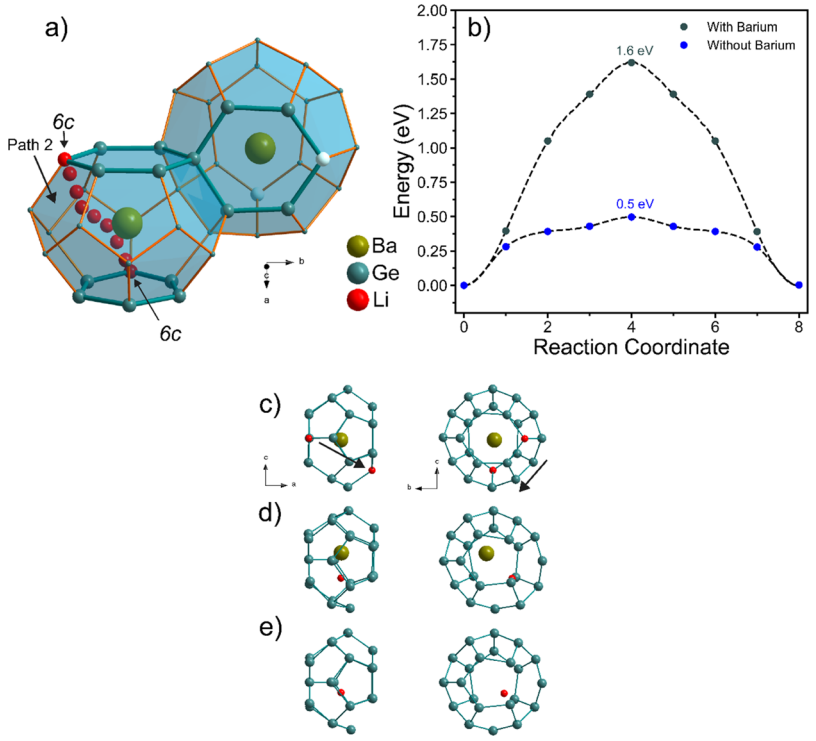

Figure 9. (a) Schematic of two connected tetrakaidecahedra showing the Li positions of Path 2 between vacancy positions within a single tetrakaidecahedron (white atom represents unfilled vacancy) (b) NEB energies of Path 2 from one vacancy to another vacancy in $Ba_8Ge_{43}\square_2Li_1$ with and without barium inside the Ge_{24} cage. (c) Schematic of a single tetrakaidecahedron with the two vacancies in each hexagonal face filled with Li (red atoms) showing the ending and starting images of the NEB calculation of Path 2. Arrows show the direction of Li movement. (d) Schematic of the highest energy image in (b) with Ba in the Ge_{24} cage. (e) Schematic of the highest energy image in (b) when Ba is not in the Ge_{24} cage.

potential Li positions in the structure were considered; if energetically favorable (with respect to bcc Li). the Li migration barriers between them were then evaluated. The formation energies, Gibbs free energy change, average lithiation voltages, and lattice constants of simulated lithiated compositions are displayed in Table 2 and schematics of these structures are displayed in Figures S12 and S13. The composition $Ba_8Ge_{43}\square_3$ means that the 6c framework vacancies are unoccupied while $Ba_8Ge_{43}\square_2Li_1$ means that 1 Li occupies one of the 6c sites in place of the vacancy. The $Ba_8Ge_{43}\square_2Li_1$ structure (Figure S12a) is found to be energetically favorable, resulting in a decrease in the formation energy and a high average lithiation voltage of 0.85 V versus Li/Li^+. Filling the three vacancies with Li (i.e., $Ba_8Ge_{43}Li_3$, Figure S12b) is also favorable with an average lithiation voltage of 0.77 V. The formation energy of these compounds also decreases with Li incorporation, indicating a stabilization of Li in the clathrate structure with respect to bcc Li. This is consistent with experimental findings that type I clathrates can be synthesized with Li in the framework positions,[35,66] suggesting that Ba_8Ge_{43} could also be synthesized with Li in these positions. Further, according to the results in Table 2, a lattice parameter increase is calculated with framework Li incorporation, which is consistent with experimental results reported by others. For example, the lattice constants of K_8Ge_{44} and $K_8Li_2Ge_{44}$ are 10.677 and 10.735 Å, respectively.[36] The calculated lattice parameter increase is ~0.2 Å for Li filling all three vacancies in $Ba_8Ge_{43}\square_3$, which should be detectable by XRD. However, no lattice constant increase was observed in our PXRD measurements at different points in lithiation

DOI: 10.1021/acsami.8b11509
ACS Appl. Mater. Interfaces 2018, 10, 37981−37993

(Figure 6b), suggesting no bulk incorporation of Li into the vacancies. Further, SCXRD measurements of lithiated samples showed no changes in lattice constant or any of the refined metrics (Supporting Information).

Next, the nudged band elastic band (NEB) method was used to assess potential pathways for bulk Li diffusion within the $Ba_8Ge_{43}\square_2Li_1$ structure through the estimation of energy barriers for Li migration. The vacancy positions reside on the hexagonal faces of the Ge_{24} cages and are rotated by 90° relative to adjacent hexagonal faces. One possible pathway, denoted as Path 1 in Figure 8a, is for Li to move to the next closest vacancy along the same chain of connected hexagons. This path involves Li moving through the hexagonal face of the Ge_{24} cage until it reaches the center position, which is the 6b site; then, the Li traverses through a pentagonal face connecting the Ge_{24} cages and follows a symmetrical pathway to the 6c site in the adjacent Ge_{24} cage that houses the other vacancy position, also via a 6b site (Video S1). Another pathway, which is more direct and denoted as Path 2 in Figure 9a, is for Li to move within a Ge_{24} cage to the vacancy site on the other hexagonal face (Video S2).

The calculated energy barriers for Path 1 and Path 2 are presented in Figures 8b and 9b, respectively, with the images for each pathway labeled in Figure S14 according to each respective reaction coordinate number. We find that the highest energy barrier between two Li vacancy sites via Path 1 is 2.1 eV. There is a local energy minimum when Li is at the 6b site; the highest energy barrier is found when Li is moved to a position off a pentagon inside the Ge_{24} cage (image 5 in Figure S14a). For Path 2, the energy barrier between the two vacancy sites is 1.6 eV, where the saddle point occurs when the Li is above a Ge−Ge bridge position between two pentagons (image 4 in Figure S14b). Both paths involve the movement of Li around the Ba guest atom inside the Ge_{24} cage, and the highest energy positions arise in both when Ba is displaced from its favorable position in the center of the cavity, incurring a high energetic cost. Figure 9c shows a single Ge_{24} cage looking down the *b*-axis (left) and *a*-axis (right) with Li (red atoms) in the 6c vacancy sites and the arrow indicating Path 2. Figure 9d shows the structure corresponding to the highest energy image from the NEB calculation, where the displacement of the Ba from the center is clearly seen. If, however, the Ba atom is absent from the cage center, the energy barrier for Li movement between the vacancies decreases to 0.5 eV (Figure 9b) and the Li is positioned closer to the cage center (Figure 9e, Video S3). As the Li diffusion barrier in c-Si is 0.47 eV[67,68] and that for c-Ge is 0.35 eV,[68] these results suggest that Li movement through the clathrate structure could be feasible but that guest atoms in the cage cavities impede lithium movement between framework vacancies. Despite lithiation into the vacancies at the 6c positions being energetically favorable, the high-energy barrier between them (1.6 or 2.1 eV, depending on the pathway) would prevent these positions from being occupied through electrochemical lithiation at room temperature.

Other Li positions aside from the framework vacancies in Ba_8Ge_{43} and $Ba_8Al_{16}Ge_{30}$ were also considered and shown in Table 2. For the Ba_8Si_{46} clathrates, the most favorable position for Li was found to be the 6b site, where the Li is centered within the hexagonal plane separating two Si_{24} cages.[25] This is also found to be the lowest energy position in the Al0 and Al16 Ge clathrates (Figure S13). However, the formation energy relative to the starting structure increased when placing Li in the 6b site, and the calculated lithiation voltages were negative. This indicates that lithiation relative to metallic Li is not energetically favorable. This was also seen in the Ba_8Si_{46} case,[25] but with a lower voltage of −1.23 V compared with −0.48 V for the Al0 Ge clathrate.

Much like the high-energy transition state between two vacancies, the instability of these positions can be rationalized by unfavorable guest atom displacements. When Li is relaxed at the 6b position in $Ba_8Al_{16}Ge_{30}$ (Figure S13a), the two Ba atoms in the adjacent cages are pushed 0.35 Å away from the cage center, resulting in a 3.1 Å Ba−Li distance. The other local minimum position found was in the $[Ge/Al]_{24}$ cage off-plane of the pentagon adjacent to the $[Ge/Al]_{20}$ cage (Figure S13b). This configuration had 0.1 eV higher energy than Li in the 6b position and resulted in the Ba atom to be pushed 0.78 Å off center, resulting in a 3.07 Å Ba−Li distance. In contrast, Li in the framework vacancies in Ba_8Ge_{43} results in no Ba displacement from the center and a Ba−Li distance of 3.84 Å. When Li is added to the 6b site in $Ba_8Ge_{43}Li_3$, the relaxed structure has large distortions in the framework as seen in Figure S12d. The voltage (−0.10 V) is higher when the vacancies are not filled (−0.48 V) suggesting that the framework distortions are more energetically favorable. This Li-induced framework distortion could lead to eventual framework destruction with the introduction of more Li where Ge−Ge bonds are broken to form the phase front of the amorphous transition, similar to what has been predicted in c-Si.[69]

It is interesting to note that Li insertion at the 6b site in Ge clathrate does seem to be more favorable than the Si clathrate case as the voltage is higher (−0.48 V vs −1.23 V). This could suggest that the Ge framework more favorably accommodates Ba displacements (resulting from Li insertion) because of the larger cage size or different framework stiffness. Previously, ab initio molecular dynamics studies have shown that Ge atoms migrate significantly during lithiation of diamond cubic Ge, whereas Si atoms remain in a static position during lithiation.[70,71] The structural rigidity of Si frameworks and limited Si migration during lithiation compared to Ge could also explain the significant difference of lithiation between Si clathrates and Ge clathrates. This is consistent with our experimental XPS, XRD, and TEM results showing that Ge clathrates are less structurally stable than the Si analogues. Overall, we find that unfavorable Li positions in the Ge clathrates and high-energy barriers between vacancies suggest that Li insertion into the crystal structure is not feasible, which is consistent with experimental results.

4. CONCLUSIONS

We investigated a series of $Ba_8Al_yGe_{46-y}$ (y = 0, 4, 8, 12, 16) type I clathrates as Li-ion battery anodes for the first time. Similar to diamond cubic Si and Ge, but different from the silicon clathrate analogues investigated in our previous studies, the Ge clathrates underwent conversion reactions to Li-rich amorphous phases. Increasing the amount of Al substitution for Ge in the clathrate resulted in a decrease in framework vacancies, a decrease in the lithiation capacity, and a reduction in the two-phase reaction voltage. Ba_8Ge_{43} reacted at ∼0.2 V versus Li/Li^+ with a capacity of 1098 mA h/g, and $Ba_8Al_{16}Ge_{30}$ reacted at 0.08 V with a capacity of 518 mA h/g. Ball-milling the hand-ground powders resulted in significant amorphization of the Ge clathrates, which led to more sloped voltage profiles characteristic of electrochemical lithiation of amorphous

DOI: 10.1021/acsami.8b11509
ACS Appl. Mater. Interfaces 2018, 10, 37981−37993

phases. Galvanostatic cycling demonstrated capacity fading typical of unoptimized Li-alloy electrodes, consistent with large volume changes and particle decrepitation during the reactions. The EIS analysis at low frequency supports the presence of a Warburg diffusion mechanism, which we attribute to bulk Li diffusion in the amorphous phases. DFT calculations were used to determine whether Li insertion and diffusion in the bulk structure is feasible. It was found that Li insertion at framework vacancies of Ba_8Ge_{43} at the 6c position is energetically favorable, but a high-energy barrier (1.6 eV) would prevent Li diffusion between vacancies unless the Ba guest atom is absent. A lattice constant increase is calculated for $Ba_8Ge_{43}Li_3$ but not observed experimentally during lithiation, suggesting no Li incorporation into the bulk clathrate structure. Overall, the bulk type I $Ba_8Al_yGe_{46-y}$ clathrates seem to be electrochemically inactive until they are converted to amorphous phases.

These results are similar to the type I Si clathrates that we previously investigated. However, the Si clathrates did not undergo a two-phase reaction to an amorphous phase, indicating that the structure is stable under these potentials. Future studies will explore the origin of the electrochemically induced amorphization observed in the type I Ge clathrates, but it could be due to the apparent greater instability of the Ge structures (e.g., to air oxidation, ball-milling) compared with the Si analogues. It could also be due to the higher stabilization of Li in Ge phases compared with Si (as indicated by higher reaction voltages for Ge). Understanding the nature of the amorphous phase transition in these intermetallic-type compounds could aid in the identification of new, stable Li-ion anodes that do not suffer from large volume expansions due to electrochemical alloying with lithium.

■ ASSOCIATED CONTENT

Supporting Information

The Supporting Information is available free of charge on the ACS Publications website at DOI: 10.1021/acsami.8b11509.

Crystallographic data for Al0 after chemical lithiation with electrolyte (TXT)

Crystallographic data for Al0 after chemical lithiation without electrolyte (TXT)

Crystallographic data for Al0 (CIF)

Crystallographic data for Al4 (CIF)

Crystallographic data for Al8 (CIF)

Crystallographic data for Al12 (CIF)

Crystallographic data for Al14 (CIF)

Crystallographic data for Al16 (CIF)

Experimental synthesis methods and characterization details; cell parameters for clathrate samples from PXRD; PXRD patterns after ball-milling for 40 min; PXRD patterns for ball-milled electrodes before and after lithiation; high-resolution Ge 2p and Al 2p XPS of clathrate electrodes; Ge 2p XPS peak area percentages; SEM of HG and BM electrodes; voltage profiles for first 5 cycles for HG-Al0; capacity versus cycle number under galvanostatic cycling for HG samples; CE of first cycle for HG and BM samples; CE of first 20 cycles for HG samples; differential capacity plots of first 3 cycles for select samples; capacity retention versus cycle number for BM-Ge; theoretical and experimental conversion capacities for Ge clathrates; voltage profile of galvanostatic testing procedures for EIS measurements; Nyquist plots for select samples; computational methods; crystal model schematics for Al0 compounds in Table 2; Li diffusion pathways with labelled images; descriptions of supporting videos of Li diffusion paths (PDF)

Supporting Video S1 (AVI)

Supporting Video S2 (AVI)

Supporting Video S3 (AVI)

■ AUTHOR INFORMATION

Corresponding Author

*E-mail: candace.chan@asu.edu. Phone: (480) 727-8614.

ORCID

J. Mark Weller: 0000-0003-2056-8974

Svilen Bobev: 0000-0002-0780-4787

Candace K. Chan: 0000-0003-4329-4865

Author Contributions

The manuscript was written through contributions of all authors. R.Z. and S.B. performed the synthesis. A.D. and R.Z. prepared the electrodes, performed the electrochemical measurements, XRD, SEM, and XPS analysis. J.M.W. performed the TEM measurements and S.B. performed the SCXRD. A.D. and X.P. performed the DFT calculations. C.K.C. conceived the project and assisted with the electrochemical analysis. All authors have given approval to the final version of the manuscript.

Notes

The authors declare no competing financial interest.

■ ACKNOWLEDGMENTS

This work was supported by funding from NSF DMR-1206795, NSF DMR-1710017, and NSF DMR-1709813. A.D. and J.M.W. acknowledge the support from ASU Fulton Schools of Engineering Dean's Fellowships. The authors greatly acknowledge the use of facilities within the Eyring Materials Center at Arizona State University. We also acknowledge the ASU Advanced Computing Center for providing computational resources on the Saguaro and Agave Clusters.

■ REFERENCES

(1) Kasper, J. S.; Hagenmuller, P.; Pouchard, M.; Cros, C. Clathrate Structure of Silicon Na_8Si_{46} and Na_xSi_{136} (x < 11). *Science* **1965**, *150*, 1713−1714.

(2) Cros, C.; Pouchard, M.; Hagenmuller, P. Sur une nouvelle famille de clathrates minéraux isotypes des hydrates de gaz et de liquides. Interprétation des résultats obtenus. *J. Solid State Chem.* **1970**, *2*, 570−581.

(3) Kawaji, H.; Horie, H.-o.; Yamanaka, S.; Ishikawa, M. Superconductivity in the Silicon Clathrate Compound $(Na, Ba)_xSi_{46}$. *Phys. Rev. Lett.* **1995**, *74*, 1427−1429.

(4) Reny, E.; San-Miguel, A.; Guyot, Y.; Masenelli, B.; Mélinon, P.; Saviot, L.; Yamanaka, S.; Champagnon, B.; Cros, C.; Pouchard, M.; Borowski, M.; Dianoux, A. Vibrational Modes in Silicon Clathrate Compounds: A Key to Understanding Superconductivity. *Phys. Rev. B: Condens. Matter Mater. Phys.* **2002**, *66*, 014532.

(5) Connétable, D.; Timoshevskii, V.; Masenelli, B.; Beille, J.; Marcus, J.; Barbara, B.; Saitta, A. M.; Rignanese, G.-M.; Mélinon, P.; Yamanaka, S.; Blase, X. Superconductivity in Doped sp^3 Semiconductors: The Case of the Clathrates. *Phys. Rev. Lett.* **2003**, *91*, 247001.

(6) Fukuoka, H.; Kiyoto, J.; Yamanaka, S. Superconductivity and Crystal Structure of the Solid Solutions of $Ba_{8-\delta}Si_{46-x}Ge_x$ ($0 \le x \le 23$)

DOI: 10.1021/acsami.8b11509
ACS Appl. Mater. Interfaces 2018, 10, 37981−37993

with Type I Clathrate Structure. *J. Solid State Chem.* **2003**, *175*, 237−244.
(7) Bryan, J. D.; Srdanov, V. I.; Stucky, G. D.; Schmidt, D. Superconductivity in Germanium Clathrate $Ba_8Ga_{16}Ge_{30}$. *Phys. Rev. B: Condens. Matter Mater. Phys.* **1999**, *60*, 3064−3067.
(8) Blake, N. P.; Mollnitz, L.; Kresse, G.; Metiu, H. Why Clathrates Are Good Thermoelectrics: A Theoretical Study of $Sr_8Ga_{16}Ge_{30}$. *J. Chem. Phys.* **1999**, *111*, 3133−3144.
(9) Nolas, G. S.; Slack, G. A.; Schujman, S. B. Chapter 6 Semiconductor Clathrates: A Phonon Glass Electron Crystal Material with Potential for Thermoelectric Applications. *Semicond. Semimetals* **2001**, *69*, 255−300.
(10) Tsujii, N.; Roudebush, J. H.; Zevalkink, A.; Cox-Uvarov, C. A.; Jeffery Snyder, G.; Kauzlarich, S. M. Phase Stability and Chemical Composition Dependence of the Thermoelectric Properties of the Type-I Clathrate $Ba_8Al_xSi_{46-x}$ ($8\leq x\leq 15$). *J. Solid State Chem.* **2011**, *184*, 1293−1303.
(11) Saramat, A.; Svensson, G.; Palmqvist, A. E. C.; Stiewe, C.; Mueller, E.; Platzek, D.; Williams, S. G. K.; Rowe, D. M.; Bryan, J. D.; Stucky, G. D. Large Thermoelectric Figure of Merit at High Temperature in Czochralski-Grown Clathrate $Ba_8Ga_{16}Ge_{30}$. *J. Appl. Phys.* **2006**, *99*, 023708.
(12) Nolas, G. S.; Cohn, J. L.; Slack, G. A.; Schujman, S. B. Semiconducting Ge Clathrates: Promising Candidates for Thermoelectric Applications. *Appl. Phys. Lett.* **1998**, *73*, 178−180.
(13) Zhang, H.; Borrmann, H.; Oeschler, N.; Candolfi, C.; Schnelle, W.; Schmidt, M.; Burkhardt, U.; Baitinger, M.; Zhao, J.-T.; Grin, Y. Atomic Interactions in the P-Type Clathrate I $Ba_8Au_{5.3}Ge_{40.7}$. *Inorg. Chem.* **2011**, *50*, 1250−1257.
(14) Uemura, T.; Akai, K.; Koga, K.; Tanaka, T.; Kurisu, H.; Yamamoto, S.; Kishimoto, K.; Koyanagi, T.; Matsuura, M. Electronic Structure and Thermoelectric Properties of Clathrate Compounds $Ba_8Al_xGe_{46-x}$. *J. Appl. Phys.* **2008**, *104*, 013702.
(15) Mott, N. F. Properties of Compounds of Type Na_xSi_{46} and Na_xSi_{136}. *J. Solid State Chem.* **1973**, *6*, 348−351.
(16) Kawaguchi, T.; Tanigaki, K.; Yasukawa, M. Ferromagnetism in Germanium Clathrate: $Ba_8Mn_2Ge_{44}$. *Appl. Phys. Lett.* **2000**, *77*, 3438−3440.
(17) Neiner, D.; Okamoto, N. L.; Condron, C. L.; Ramasse, Q. M.; Yu, P.; Browning, N. D.; Kauzlarich, S. M. Hydrogen Encapsulation in a Silicon Clathrate Type I Structure: $Na_{5.5}(H_2)_{2.15}Si_{46}$: Synthesis and Characterization. *J. Am. Chem. Soc.* **2007**, *129*, 13857−13862.
(18) Neiner, D.; Okamoto, N. L.; Yu, P.; Leonard, S.; Condron, C. L.; Toney, M. F.; Ramasse, Q. M.; Browning, N. D.; Kauzlarich, S. M. Synthesis and Characterization of $K_{8-x}(H_2)_ySi_{46}$. *Inorg. Chem.* **2010**, *49*, 815−822.
(19) San-Miguel, A.; Kéghélian, P.; Blase, X.; Mélinon, P.; Perez, A.; Itié, J. P.; Polian, A.; Reny, E.; Cros, C.; Pouchard, M. High Pressure Behavior of Silicon Clathrates: A New Class of Low Compressibility Materials. *Phys. Rev. Lett.* **1999**, *83*, 5290−5293.
(20) San-Miguel, A.; Toulemonde, P. High-Pressure Properties of Group IV Clathrates. *High Pressure Res.* **2005**, *25*, 159−185.
(21) Langer, T.; Dupke, S.; Trill, H.; Passerini, S.; Eckert, H.; Pöttgen, R.; Winter, M. Electrochemical Lithiation of Silicon Clathrate-II. *J. Electrochem. Soc.* **2012**, *159*, A1318−A1322.
(22) Yang, J.; Tse, J. S. Silicon Clathrates as Anode Materials for Lithium Ion Batteries? *J. Mater. Chem. A* **2013**, *1*, 7782.
(23) Wagner, N. A.; Raghavan, R.; Zhao, R.; Wei, Q.; Peng, X.; Chan, C. K. Electrochemical Cycling of Sodium-Filled Silicon Clathrate. *ChemElectroChem* **2014**, *1*, 347−353.
(24) Li, Y.; Raghavan, R.; Wagner, N. A.; Davidowski, S. K.; Baggetto, L.; Zhao, R.; Cheng, Q.; Yarger, J. L.; Veith, G. M.; Ellis-Terrell, C.; Miller, M. A.; Chan, K. S.; Chan, C. K. Type I Clathrates as Novel Silicon Anodes: An Electrochemical and Structural Investigation. *Adv. Sci.* **2015**, *2*, 1500057.
(25) Peng, X.; Wei, Q.; Li, Y.; Chan, C. K. First-Principles Study of Lithiation of Type i Ba-Doped Silicon Clathrates. *J. Phys. Chem. C* **2015**, *119*, 28247−28257.
(26) Chan, K. S.; Miller, M. A.; Liang, W.; Ellis-Terrell, C.; Chan, C. K. First Principles and Experimental Studies of Empty Si_{46} as Anode Materials for Li-Ion Batteries. *J. Mater. Res.* **2016**, *31*, 3657−3665.
(27) Warrier, P.; Koh, C. A. Silicon Clathrates for Lithium Ion Batteries: A Perspective. *Appl. Phys. Rev.* **2016**, *3*, 040805.
(28) Böhme, B.; Bonatto Minella, C.; Thoss, F.; Lindemann, I.; Rosenburg, M.; Pistidda, C.; Møller, K. T.; Jensen, T. R.; Giebeler, L.; Baitinger, M.; Gutfleisch, O.; Ehrenberg, H.; Eckert, J.; Grin, Y.; Schultz, L. B1-Mobilstor: Materials for Sustainable Energy Storage Techniques - Lithium Containing Compounds for Hydrogen and Electrochemical Energy Storage. *Adv. Eng. Mater.* **2014**, *16*, 1189−1195.
(29) Zhao, R.; Bobev, S.; Krishna, L.; Yang, T.; Weller, J. M.; Jing, H.; Chan, C. K. Anodes for Lithium-Ion Batteries Based on Type I Silicon Clathrate $Ba_8Al_{16}Si_{30}$ - Role of Processing on Surface Properties and Electrochemical Behavior. *ACS Appl. Mater. Interfaces* **2017**, *9*, 41246−41257.
(30) Huggins, R. A.; Nix, W. D. Decrepitation Model for Capacity Loss during Cycling of Alloys in Rechargeable Electrochemical Systems. *Ionics* **2000**, *6*, 57−63.
(31) Gou, W.; Rodriguez, S. Y.; Li, Y.; Ross, J. H. NMR Experiments and Electronic Structure Calculations in Type-I BaAlGe Clathrates. *Phys. Rev. B: Condens. Matter Mater. Phys.* **2009**, *80*, 144108.
(32) Rodriguez, S. Y.; Saribaev, L.; Ross, J. H. Zintl Behavior and Vacancy Formation in Type-I Ba-Al-Ge Clathrates. *Phys. Rev. B: Condens. Matter Mater. Phys.* **2010**, *82*, 064111.
(33) Schäfer, H.; Eisenmann, B.; Müller, W. Zintl Phases: Transitions between Metallic and Ionic Bonding. *Angew. Chem., Int. Ed.* **1973**, *12*, 694−712.
(34) Carrillo-Cabrera, W.; Budnyk, S.; Prots, Y.; Grin, Y. Ba_8Ge_{43} Revisited: A 2a′ x 2a′ x 2a′ Superstructure of the Clathrate-I Type with Full Vacancy Ordering. *Z. Anorg. Allg. Chem.* **2004**, *630*, 2267−2276.
(35) Böhme, B.; Bobnar, M.; Ormeci, A.; Peters, S.; Schnelle, W.; Baitinger, M.; Grin, Y. Type-I Silicon Clathrates Containing Lithium. *Z. Kristallogr.—Cryst. Mater.* **2017**, *232*, 223−233.
(36) Liang, Y.; Böhme, B.; Ormeci, A.; Borrmann, H.; Pecher, O.; Haarmann, F.; Schnelle, W.; Baitinger, M.; Grin, Y. A Clathrate-I Phase with Li-Ge Framework. *Chem.—Eur. J.* **2012**, *18*, 9818−9822.
(37) Böhme, B.; Wei, K.; Bobnar, M.; Prots, Y.; Burkhardt, U.; Baitinger, M.; Nolas, G. S.; Grin, Y. A Type-II Clathrate with a Li-Ge Framework. *Z. Kristallogr.—Cryst. Mater.* **2017**, *232*, 543−556.
(38) Obrovac, M. N.; Christensen, L. Structural Changes in Silicon Anodes during Lithium Insertion/Extraction. *Electrochem. Solid-State Lett.* **2004**, *7*, A93−A96.
(39) Loaiza, L. C.; Louvain, N.; Fraisse, B.; Boulaoued, A.; Iadecola, A.; Johansson, P.; Stievano, L.; Seznec, V.; Monconduit, L. Electrochemical Lithiation of Ge: New Insights by Operando Spectroscopy and Diffraction. *J. Phys. Chem. C* **2018**, *122*, 3709−3718.
(40) Lim, L. Y.; Liu, N.; Cui, Y.; Toney, M. F. Understanding Phase Transformation in Crystalline Ge Anodes for Li-Ion Batteries. *Chem. Mater.* **2014**, *26*, 3739−3746.
(41) Jung, H.; Allan, P. K.; Hu, Y.-Y.; Borkiewicz, O. J.; Wang, X.-L.; Han, W.-Q.; Du, L.-S.; Pickard, C. J.; Chupas, P. J.; Chapman, K. W.; Morris, A. J.; Grey, C. P. Elucidation of the Local and Long-Range Structural Changes that Occur in Germanium Anodes in Lithium-Ion Batteries. *Chem. Mater.* **2015**, *27*, 1031−1041.
(42) Henkelman, G.; Uberuaga, B. P.; Jónsson, H. A Climbing Image Nudged Elastic Band Method for Finding Saddle Points and Minimum Energy Paths. *J. Chem. Phys.* **2000**, *113*, 9901−9904.
(43) Condron, C. L.; Porter, R.; Guo, T.; Kauzlarich, S. M. Crystal Structures, Raman Spectroscopy, and Magnetic Properties of $Ba_{7.5}Al_{13}Si_{29}$ and $Eu_{0.27}Ba_{7.22}Al_{13}Si_{29}$. *Inorg. Chem.* **2005**, *44*, 9185−9191.
(44) Condron, C. L.; Martin, J.; Nolas, G. S.; Piccoli, P. M. B.; Schultz, A. J.; Kauzlarich, S. M. Structure and Thermoelectric Characterization of $Ba_8Al_{14}Si_{31}$. *Inorg. Chem.* **2006**, *45*, 9381−9386.

DOI: 10.1021/acsami.8b11509
ACS Appl. Mater. Interfaces 2018, 10, 37981−37993

(45) Bobnar, M.; Böhme, B.; Wedel, M.; Burkhardt, U.; Ormeci, A.; Prots, Y.; Drathen, C.; Liang, Y.; Nguyen, H. D.; Baitinger, M.; Grin, Y. Distribution of Al Atoms in the Clathrate-I Phase $Ba_8Al_xSi_{46-x}$ at x = 6.9. *Dalton Trans.* **2015**, *44*, 12680−12687.
(46) Roudebush, J. H.; de la Cruz, C.; Chakoumakos, B. C.; Kauzlarich, S. M. Neutron Diffraction Study of the Type I Clathrate $Ba_8Al_xSi_{46-x}$: Site Occupancies, Cage Volumes, and the Interaction between the Guest and the Host Framework. *Inorg. Chem.* **2012**, *51*, 1805−1812.
(47) Aydemir, U.; Candolfi, C.; Borrmann, H.; Baitinger, M.; Ormeci, A.; Carrillo-Cabrera, W.; Chubilleau, C.; Leonir, B.; Dauscher, A.; Oeschler, N.; Steglich, F.; Grin, Y. Crystal Structure and Transport Properties of $Ba_8Ge_{43}\square_3$. *Dalton Trans.* **2010**, *39*, 1078−1088.
(48) Okamoto, N. L.; Oh, M. W.; Nishii, T.; Tanaka, K.; Inui, H. Crystal Structure and Thermoelectric Properties of the Type-I Clathrate Compound Ba_8Ge_{43} with an Ordered Arrangement of Ge Vacancies. *J. Appl. Phys.* **2006**, *99*, 033513.
(49) Prabhakaran, K.; Ogino, T. Oxidation of Ge(100) and Ge(111) Surfaces: An UPS and XPS Study. *Surf. Sci.* **1995**, *325*, 263−271.
(50) Kume, T.; Ban, T.; Ohashi, F.; Jha, H. S.; Sugiyama, T.; Ogura, T.; Sasaki, S.; Nonomura, S. A Thin Film of a Type II Ge Clathrate Epitaxially Grown on a Ge Substrate. *CrystEngComm* **2016**, *18*, 5630−5638.
(51) Alexander, M. R.; Thompson, G. E.; Beamson, G. Characterization of the Oxide/Hydroxide Surface of Aluminium Using X-ray Photoelectron Spectroscopy: A Procedure for Curve Fitting the O 1s Core Level. *Surf. Interface Anal.* **2000**, *29*, 468−477.
(52) Huggins, R. A. Materials Science Principles Related to Alloys of Potential Use in Rechargeable Lithium Cells. *J. Power Sources* **1989**, *26*, 109−120.
(53) Chockla, A. M.; Klavetter, K. C.; Mullins, C. B.; Korgel, B. A. Solution-Grown Germanium Nanowire Anodes for Lithium-Ion Batteries. *ACS Appl. Mater. Interfaces* **2012**, *4*, 4658−4664.
(54) Graetz, J.; Ahn, C. C.; Yazami, R.; Fultz, B. Nanocrystalline and Thin Film Germanium Electrodes with High Lithium Capacity and High Rate Capabilities. *J. Electrochem. Soc.* **2004**, *151*, A698−A702.
(55) Hatchard, T. D.; Dahn, J. R. In Situ XRD and Electrochemical Study of the Reaction of Lithium with Amorphous Silicon. *J. Electrochem. Soc.* **2004**, *151*, A838−A842.
(56) Liu, C.; Neale, Z. G.; Cao, G. Understanding Electrochemical Potentials of Cathode Materials in Rechargeable Batteries. *Mater. Today* **2016**, *19*, 109−123.
(57) Ryu, J. H.; Kim, J. W.; Sung, Y.-E.; Oh, S. M. Failure Modes of Silicon Powder Negative Electrode in Lithium Secondary Batteries. *Electrochem. Solid-State Lett.* **2004**, *7*, A306−A309.
(58) Yoon, S.; Park, C.-M.; Sohn, H.-J. Electrochemical Characterizations of Germanium and Carbon-Coated Germanium Composite Anode for Lithium-Ion Batteries. *Electrochem. Solid-State Lett.* **2008**, *11*, A42−A45.
(59) Klavetter, K. C.; Wood, S. M.; Lin, Y.-M.; Snider, J. L.; Davy, N. C.; Chockla, A. M.; Romanovicz, D. K.; Korgel, B. A.; Lee, J.-W.; Heller, A.; Mullins, C. B. A High-Rate Germanium-Particle Slurry Cast Li-Ion Anode with High Coulombic Efficiency and Long Cycle Life. *J. Power Sources* **2013**, *238*, 123−136.
(60) Hamon, Y.; Brousse, T.; Jousse, F.; Topart, P.; Buvat, P.; Schleich, D. M. Aluminum Negative Electrode in Lithium Ion Batteries. *J. Power Sources* **2001**, *97*−*98*, 185−187.
(61) Fleischauer, M. D.; Obrovac, M. N.; Dahn, J. R. Al-Si Thin-Film Negative Electrodes for Li-Ion Batteries. *J. Electrochem. Soc.* **2008**, *155*, A851−A854.
(62) Tillard, M.; Belin, C.; Spina, L.; Jia, Y. Z. Phase Stabilities, Electronic and Electrochemical Properties of Compounds in the LiAlSi System. *Solid State Sci.* **2005**, *7*, 1125−1134.
(63) Baggetto, L.; Notten, P. H. L. Lithium-Ion (De)Insertion Reaction of Germanium Thin-Film Electrodes: An Electrochemical and In Situ XRD Study. *J. Electrochem. Soc.* **2009**, *156*, A169−A175.
(64) Song, J.; Lee, H. H.; Wang, Y. Y.; Wan, C. C. Two- and Three-Electrode Impedance Spectroscopy of Lithium-Ion Batteries. *J. Power Sources* **2002**, *111*, 255−267.
(65) Ångqvist, M.; Erhart, P. Understanding Chemical Ordering in Intermetallic Clathrates from Atomic Scale Simulations. *Chem. Mater.* **2017**, *29*, 7554−7562.
(66) Liang, Y.; Schnelle, W.; Veremchuk, I.; Böhme, B.; Baitinger, M.; Grin, Y. Synthesis and Thermoelectric Properties of the Clathrate-I Phase $K_8Li_xGe_{44-x/4}\square_{2-3x/4}$. *J. Electron. Mater.* **2015**, *44*, 4444−4451.
(67) Chan, T.-L.; Chelikowsky, J. R. Controlling Diffusion of Lithium in Silicon Nanostructures. *Nano Lett.* **2010**, *10*, 821−825.
(68) Chou, C.-Y.; Kim, H.; Hwang, G. S. A Comparative First-Principles Study of the Structure, Energetics, and Properties of Li-M (M = Si, Ge, Sn) Alloys. *J. Phys. Chem. C* **2011**, *115*, 20018−20026.
(69) Zhao, K.; Wang, W. L.; Gregoire, J.; Pharr, M.; Suo, Z.; Vlassak, J. J.; Kaxiras, E. Lithium-Assisted Plastic Deformation of Silicon Electrodes in Lithium-Ion Batteries: A First-Principles Theoretical Study. *Nano Lett.* **2011**, *11*, 2962−2967.
(70) Chou, C.-Y.; Hwang, G. S. On the Origin of the Significant Difference in Lithiation Behavior between Silicon and Germanium. *J. Power Sources* **2014**, *263*, 252−258.
(71) Chou, C.-Y.; Hwang, G. S. On the Origin of Anisotropic Lithiation in Crystalline Silicon over Germanium: A First Principles Study. *Appl. Surf. Sci.* **2014**, *323*, 78−81.

DOI: 10.1021/acsami.8b11509
ACS Appl. Mater. Interfaces 2018, 10, 37981−37993